ADVANCED MATERIALS
www.advmat.de

Waterproof and Flexible Perovskite Photodetector Enabled By P-type Organic Molecular Rubrene with High Moisture and Mechanical Stability

Ruofei Xing, Ziqing Li, Wenxiao Zhao, Dong Wang, Ranran Xie, Yanxue Chen, Limin Wu,* and Xiaosheng Fang**

Metal halide perovskite films have gained significant attention because of their remarkable optoelectronic performances. However, their poor stability upon the severe environment appears to be one of the main facets that impedes their further commercial applications. Herein, a method to improve the stability of flexible photodetectors under water and humidity environment without encapsulation is reported. The devices are fabricated using the physical vapor deposition method (Pulse Laser Deposition & Thermal Evaporation) under high-vacuum conditions. An amorphous organic Rubrene film with low molecular polarity and high elastic modulus serves as both a protective layer and hole transport layer. After immersed in water for 6000 min, the photoluminescence intensity attenuation of films only decreased by a maximum of 10%. The demonstrator device, based on Rubrene/$CsPbBr_3$/ZnO heterojunction confirms that the strategy not only enhances device moisture and mechanical stability but also achieves high sensitivity in optoelectronic detection. In self-powered mode, it has a fast response time of 79.4 µs /207.6 µs and a responsivity 124 mA W^{-1}. Additionally, the absence of encapsulation simplifies the fabrication of complex electrodes, making it suitable for various applications. This study highlights the potential use of amorphous organic films in improving the stability of perovskite-based flexible devices.

1. Introduction

Metal halide perovskites are emerging as one of the most promising materials for optoelectronic devices, primarily due to their superior electronical and optical properties, such as high carrier mobility, tunable optical bandgap, large light absorption efficiency, and so on.[1–3] With intense investigate in the past several years, they are extensively applied to self-powered photodetectors (SPPDs), solar cells, light emitting diodes (LED) and lasers.[4–7] Although perovskite-based optoelectronic devices have made many breakthroughs in performance, they are still suffering from shortcomings in stability which present significant obstacles to commercialization.[8–10]

Improving the stability of metal halide perovskite-based devices is a complex system engineering task.[11–13] As the instability of perovskite materials is influenced by both internal and external factors.[14] Internal factors, including ion migration and structural instability, can result in changes to the physical and chemical properties of perovskite materials.[15–17] On the other hand, external factors such as residual solvents, thermal, moisture, oxidation, stress, and electric field can disrupt the crystal lattice structure of perovskite materials, thus affecting the overall performance of optoelectronic devices.[18,19] Among them, the most serious threat to the stability of the perovskites is moisture. In the perovskite structure, water molecules can easily penetrate and lead to the formation of an intermediate monohydrate

R. Xing, L. Wu, X. Fang
Department of Materials Science and State Key Laboratory of Molecular Engineering of Polymers
Fudan University
Shanghai 200433, P. R. China
E-mail: lmw@fudan.edu.cn; xshfang@fudan.edu.cn

Z. Li, X. Fang
Shanghai Frontiers Science Research Base of Intelligent Optoelectronics and Perception
Institute of Optoelectronics
Fudan University
Shanghai 200433, P. R. China

W. Zhao, D. Wang, R. Xie, Y. Chen
School of Physics
and State Key Laboratory of Crystal Materials
Shandong University
Jinan 250100, P. R. China
E-mail: cyx@sdu.edu.cn

L. Wu
College of Chemistry and Chemical Engineering Inner Mongolia University
Hohhot 010021, P. R. China

The ORCID identification number(s) for the author(s) of this article can be found under https://doi.org/10.1002/adma.202310248

DOI: 10.1002/adma.202310248

and dihydrate perovskite. Specifically, water molecules that exist within grain boundaries establish hydrogen bonds with the cations at the A site. As a result, the bond between the cation and the octahedron is weakened, facilitating the deprotonation of the A site cations. Furthermore, the process of deprotonation occurs more rapidly under the influence of external stressors, such as heat or electric fields.[20]

Various efforts have been made to mitigate the impact of moisture on device stability, with encapsulation proving to be one of the most effective approaches.[21,22] One of the mainstream methods currently used for packaging devices involves covering the surface of the device with a glass cover plate.[23] Desiccants, deoxidizers, and epoxy resin are used to fill the middle area of the cover plate and the gaps around, creating a closed space that isolates the device from the external atmosphere. While this method significantly extends the lifespan of devices, it cannot be applied to flexible devices and has some drawbacks in terms of electrode leads, device costs, and environmental protection. Additionally, applying an organic packaging adhesive to the surface of the device can protect it, but the cured adhesive may affect the mechanical stability of flexible devices.[24,25] Consequently, finding a top functional layer that can provide a packaging role without altering the original preparation process would be beneficial for improving the long-term stability of the device. To address this issue, this paper proposes the use of Rubrene.

Rubrene is known for its high hole mobility (40 cm^2 $(V \times s)^{-1}$) among organic semiconductors and is commonly used in organic light-emitting diodes (OLEDs), organic field-effect transistors, and flexible displays.[26–29] Compared to highly acclaimed single-crystal and polycrystalline thin films, amorphous Rubrene films are often overlooked due to their poor hole transfer capability.[30,31] However, amorphous thin films possess dense, boundary-free, and mildly hydrophobic features that precisely meet the requirements of encapsulation layers.[32] By optimizing the thickness of Rubrene films and combining them with ZnO films that possess strong charge carrier extraction ability, highly stable and high-performance perovskite-based photodetectors can be constructed (The optimization process is shown in the Figure S1, Supporting Information). The Rubrene film acts both as a hole transport layer, effectively separating the hole-electron pairs generated by light, and as a protective layer, protecting the perovskite material from damage caused by the external environment. In addition, the excellent flexibility of amorphous Rubrene films ensures the mechanical stability of flexible devices, making them promising for applications in wearable devices and irregularly shaped equipment. Finally, to demonstrate its ease of processing, a 10 × 10 sensors array is fabricated and its potential for imaging applications is explored.

2. Results and Discussion

To ensure that moisture does not come into contact with the inner perovskite film, it is necessary for the Rubrene film to serve as a waterproof layer by fully covering the underlying film structure. In order to achieve this, a metal mask is utilized during the deposition of the electron transport layer and perovskite films on the substrate surface, resulting in a smaller film area being deposited compared to the substrate area. Subsequently, the mask on the substrate is removed during the growth of the Rubrene film using a thermal evaporation system, allowing the Rubrene to completely cover the inner film, the preparation process diagram is shown in Figure S2, Supporting Information. As schematically shown in **Figure 1**a, vertical sandwich structure is adopted to build a device, where a perovskite film and ZnO film are covered by a Rubrene film. The schematic diagram of the final devices is shown in Figure S3, Supporting Information. The incident light is absorbed by the perovskite layer, generating device photocarriers (electrons and holes), which are rapidly extracted by the ZnO layer and the Rubrene layer, respectively, under the influence of the built-in electric field. This leads to the generation of a response signal. In this process, the Rubrene thin film acts as a hole transport layer, enhancing the extraction speed and efficiency of the photocarriers. Meanwhile, this layer prevents water molecules from entering the device, thus preserving the optical absorption of the perovskite thin film. The water resistance of the amorphous Rubrene film can be attributed to two main factors: first, Rubrene is an organic material with low polarity and has a hydrophobicity; second, the morphology of amorphous films is extremely dense and smooth, without any macroscopic grain boundaries or pinholes. The affinity between material and water can be quantified using the hydrophobic parameter.[39] Figure 1b demonstrates molecule structure of Rubrene and image of water contact angle test.[40]

As a derivative of tetracene that features four phenyl rings, Rubrene predominantly grows in an amorphous phase through thermal evaporation. Due to its high structural symmetry and weak polarity, the film has relatively low water molecule affinity, as it consists only of benzene rings and C-H bonds. Consequently, the exchange of electrons and hydrogen bonding with interfacial water molecules is less likely. This inference also finds support in the water contact angle test.

As it is well known that water molecules primarily affect the lattice structure of perovskite films. Therefore, the protective effect of Rubrene films can be investigated by analyzing the optical properties of devices. Photoluminescence spectra (PL) are employed to assess the damage caused to the perovskite films. In order to do so, water immersion tests are conducted on films consisting of $MAPbBr_3$, $(PEA)_2PbBr_4$, $CsPbBr_3$, and $FAPbI_3$ with a Rubrene coating. The PL intensity of these films is periodically measured, as depicted in Figure 1c. During the 6000-min test period, the PL intensity of all films declines gradually. The bromine-based perovskite films display a similar attenuation trend. Their PL intensity ultimately decays- to 90% of the initial value. As for the iodine-based perovskite film, its decay rate is relatively high at the beginning, but rapidly stabilized at a final intensity comparable to bromine-based perovskite. The potential cause for this outcome may lie in the varying photostability of different anionic perovskite thin films. **Table 1** presents prior waterproof performance tests conducted on optoelectronic devices that rely on perovskite thin films. In the Figure S4, Supporting Information, we also provide photos of the device immersed in water, which shows that the perovskite layer in the heterojunction is not damaged by prolonged immersion under the protection of Rubrene. Notably, amorphous Rubrene film demonstrates comparable waterproof performance to specialized packaging layers.

Rubrene/$CsPbBr_3$/ZnO heterojunctions are used as a representative device to showcase its stability in atmospheric conditions. The PL peaks of the $CsPbBr_3$ film in the heterojunction

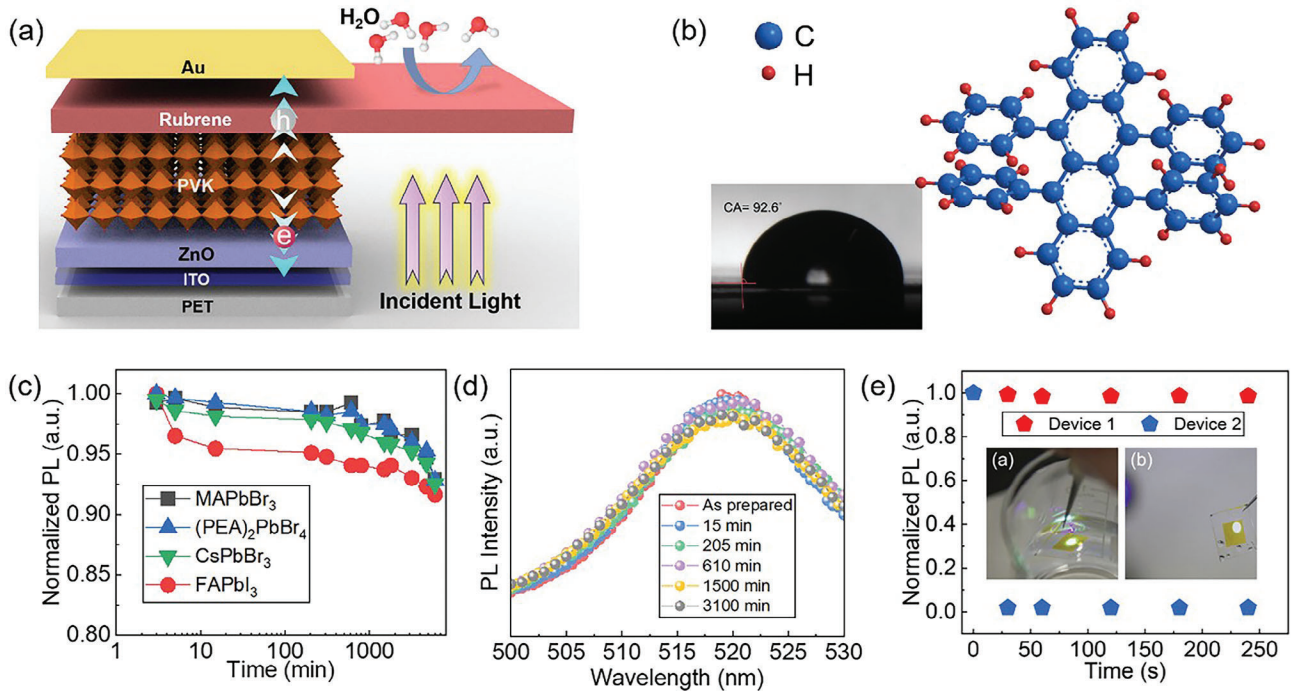

Figure 1. a) The diagram of the device structure and properties of Rubrene film. b) Molecular structure schematic and water contact angle image of Rubrene film. c) Normalized PL intensity of different perovskite films covered with Rubrene film after immersion in water. d) PL pattern of Rubrene/$CsPbBr_3$/ZnO films stored in ambient air. e) Normalized PL intensity of $CsPbBr_3$ with or without Rubrene protection.

are demonstrated in Figure 1d. It can be observed that the intensity of the characteristic fluorescence peak at 520 nm wavelength remains almost unchanged throughout the entire test duration of up to 3100 min. This finding provides strong evidence for the exceptional stability of the device in ambient air.

In order to demonstrate that Rubrene film not only protects perovskite films from water erosion but also contributes to the output performance and mechanical stability of the devices, we fabricate rubene/$CsPbBr_3$/ZnO photodetectors (Device 1) on flexible ITO/PET substrates, as well as a control group of ZnO/$CsPbBr_3$/Rubrene photodetectors (Device 2). Schematic diagrams of the devices are presented in Supporting Information (Figure S5, Supporting Information). The outermost layer of Device 1 is coated with Rubrene, while the outermost layer of Device 2 is coated with ZnO. To further validate the water protection capabilities of amorphous Rubrene films on perovskite-based devices, the devices are submerged in water and the resulting change in intensity of the characteristic peak of $CsPbBr_3$ films in the photoluminescence spectra is measured. Device 1 is able to maintain the intensity of photoluminescence for a longer period of time when immersed in water, as illustrated in Figure 1e. This indicates that the perovskite film, serving as the functional layer in Device 1, remains intact and is not damaged by water due to the protection of the Rubrene film. In contrast, Device 2, where the outermost layer is a ZnO film, immediately becomes damaged and no longer exhibits characteristic photoluminescence when exposed to water. This is evidence that the macroscopic grain boundaries provide favorable conditions for water molecules to enter the device. When operating under self-powered mode, **Figure** 2a shows that both devices exhibit similar magnitudes of photocurrent and dark current. However, a noticeable difference in the photocurrent output

Table 1. The stability characteristic of different perovskite-based optoelectrical.

Structure	Encapsulation materials	Stability test conditions	% of initial value	Refs
Glass/FTO/TiO_2/$MAPbI_3$/Spiro-OMeTAD	PI tape	1620 s/water	96.3	[33]
Glass/FTO/TiO_2/$MAPbI_3$/Spiro-OMeTAD	Adamantane nanocomposite	60 s/water	95	[34]
Glass/FTO/ZnO/MAPI/Spiro-OMeTAD	UV-curable epoxy	6 h/85 °C, 65% RH	90	[35]
Glass/FTO/TiO_2/PVK/PCBM	PZPY (Additive)	36 h/85 °C, 50% RH	90	[36]
PEN/ $FAPbI_3$/PCBM/Au	PVA (Additive)	36 h/RT, 80% RH	80	[37]
PI/Au/$CsPbBr_3$@FDTS/Au	FDTS (Additive)	10 h/85 °C, 85% RH	100	[38]
PET/ITO/ZnO/$CsPbBr_3$/Rubrene	None	100 h/water	91	this work

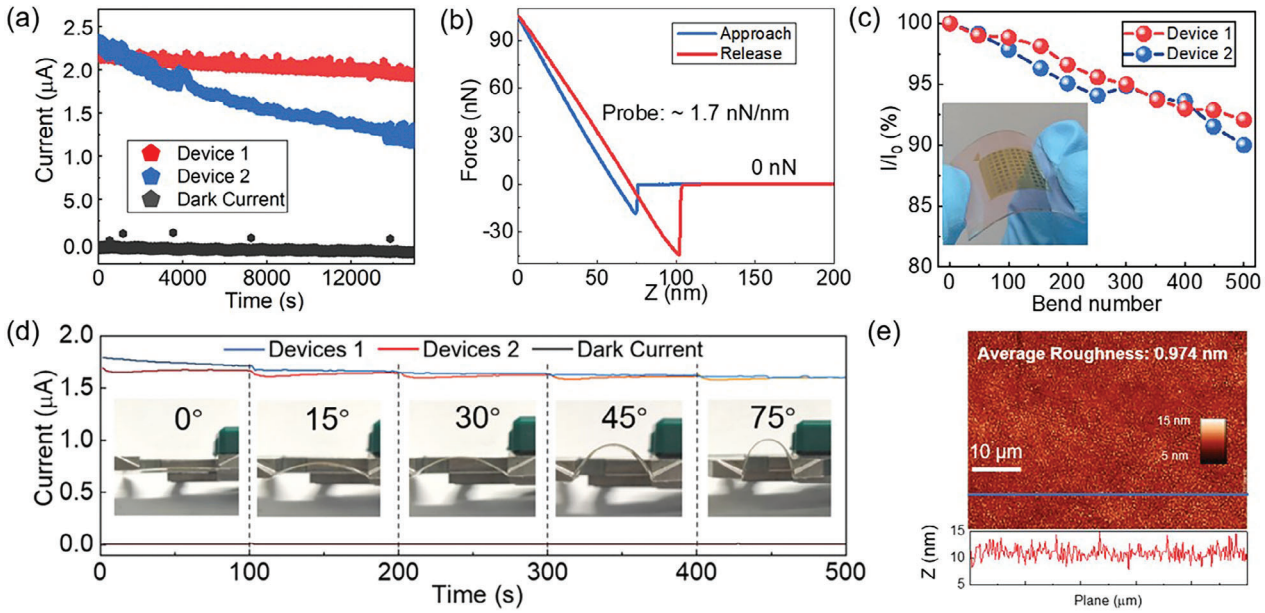

Figure 2. a) Devices output photocurrent and dark current under the 465 nm illumination (15 mW cm^{-2}) at 0 V. b) The force curve test of the Rubrene film. c) Mechanical stability test after multiple bending cycles. d) Devices output photocurrent at various bending angles. e) AFM topographical images of the device.

between the devices emerged after continuous operation for 15000 s in the same atmospheric conditions. Specifically, Device 1 demonstrates minimal decay in the photocurrent, while Device 2 displays a significant decay of up to 45%.

Rubrene films have good elasticity, allowing the construction of flexible devices with good mechanical stability and photodetection capabilities. Thus, the force curve mode of the atomic force microscope (AFM) is used to test the elastic modulus of the film as shown in Figure 2b. The blue curve (approach) represents the path of the probe during the downward movement. Initially, it is a straight line from right to left without any bending before contacting with the sample, indicating a force of 0 nN. At ≈75 nm on the x-axis, the curve suddenly drops, indicating the probe's approach toward the sample, which causes it to bend downward due to attractive forces. As the probe continues to descend, it reaches a point ≈62 nm on the x-axis where the attractive and repulsive forces balance, resulting in no bending of the probe. Beyond this point, the repulsive forces cause the probe to bend upward until it reaches 0 nm on the x-axis, where the absolute bending value of the probe is 62 nm. As the bending of the probe is linearly related to the applied force, the calculated force at 0 nm is ≈105 nN. The red curve (release) represents the reverse process. Positive force values above 0 nN represent repulsion, while negative values below 0 nN represent attraction. The elastic modulus can be determined by fitting the force curve using the Derjaguin–Muller–Toporov (DMT) model. This model relates the indentation force F to the depth d using the equation:[41]

$$F = \frac{4}{3} E^* \sqrt{R_{\text{Probe}}} d^{3/2} + F_{\text{Adh}} \quad (1)$$

where E^* is the effective modulus at the AFM probe–sample contact; R_{Probe} is the probe radius; F_{Adh} is the adhesion force an estimated to be ≈24 nN. Throughout the experiment, the AFM system employs Equation (1) to automatically fit the indentation of force curves at each location within the scanned area. As a result, topography and elasticity mapping can be accomplished simultaneously, and they are presented in Figure S6, Supporting Information. The measured elastic modulus is ≈11 GPa which is reasonable with previously reported values.[42] The high modulus of elasticity of Rubrene film can theoretically tolerate multiple bending of the flexible device without cracking, which is beneficial to the mechanical stability of the flexible device. Especially when the bending angle is large, compared to ZnO film, Rubrene film can better fit the deformation of the substrate, so that the flexible Device 2 can obtain more stable photocurrent output. However, in the mechanical stability tests of the devices in Figure 2c,d, both Device 1 and Device 2 exhibit similar photodetection capabilities.

In details, the values of the photocurrents of the devices are maintained at more than 90% of the initial values, and the photocurrent of Device 1 is also slightly higher than that of Device 2 after 500 bending cycles. Compared with state-of-the-art flexible photodetectors, the attenuation of the device is a little more pronounced. The reasons for this phenomenon are discussed in detail in the supporting information, Figure S7, Supporting Information. As illustrated in Figure 2d, the output photocurrents of the devices are relatively stable at different bending angles. This is due to the relatively thin thickness (≈400 nm) of the heterojunction. The thickness of each layer of heterojunctions is obtained via cross-sectional SEM image in Figure S8, Supporting Information. Although the elastic modulus difference between the multilayer films is large, the small thickness effectively reduces the internal stress and relative deformation between the layers under bending conditions, making the device stable and efficient in photodetection under deformation conditions. As depicted in Figure 2e, the roughness of the device's surface is

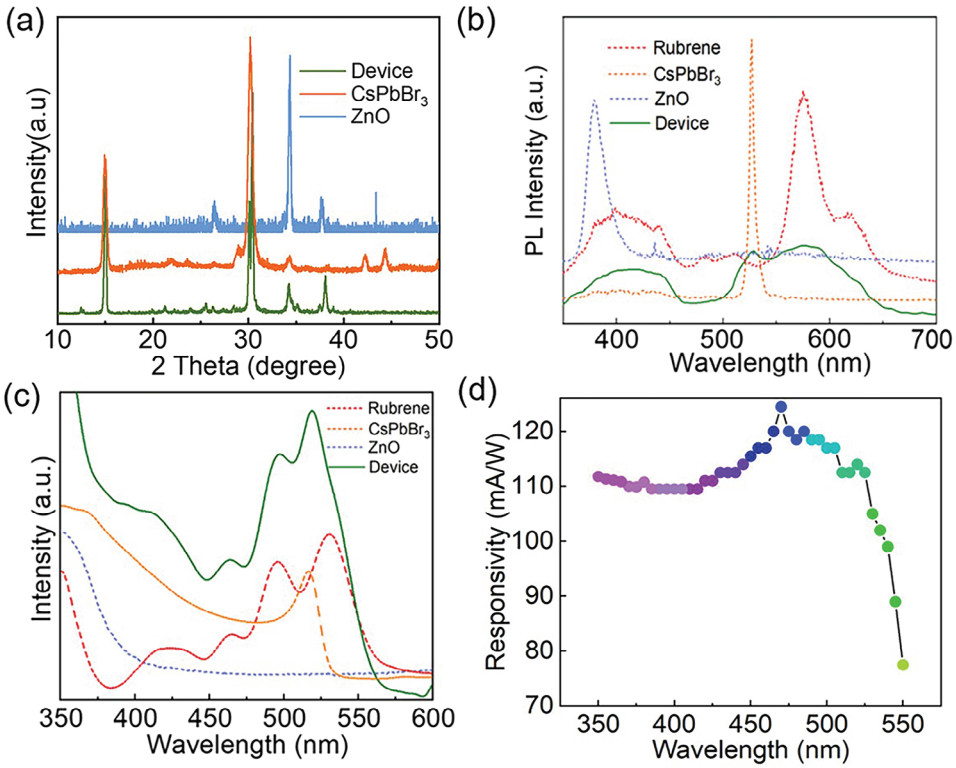

Figure 3. a) XRD pattern of polycrystalline $CsPbBr_3$ film, ZnO film and as-prepared device. b) PL pattern and c) Absorption spectra of each film in device. d) The responsivity of SPPD under the UV–vis light.

evaluated via AFM measurements. Due to the ultra-low surface roughness of ITO/PET substrates (Figure S9, Supporting Information), the surface morphology of the device is very dense and flat. The roughness value is about 1 nm, indicating that the surface of the amorphous Rubrene film is smooth and free of macroscopic grain boundaries.

In addition, X-ray diffraction (XRD) analysis is conducted to assess the crystalline quality and lattice structure of polycrystalline films in device. As shown in **Figure** 3a, the green curve displays three distinct diffraction peaks. Among these peaks, the ones at 15° and 30° are similar in terms of height and width, indicating that they are the characteristic diffraction peaks of the $CsPbBr_3$ film. The peak near 34.4° stands out as being noticeably different, suggesting that it corresponds to the characteristic diffraction peaks of the ZnO film. As for the Rubrene film deposited via thermal evaporation, being an amorphous film, it lacks any characteristic diffraction peaks. In order to highlight the characteristic diffraction peaks of $CsPbBr_3$ and ZnO films, we further prepare $CsPbBr_3$ film and ZnO film using the same growth conditions on ITO/PET substrates, respectively. Subsequently, we characterize them individually using XRD, with the results shown as the orange and purple curves. The orange curve, when compared to the standard data card PDF#54-0752, corresponds to the $CsPbBr_3$ material with a space group of Pm-3m. Specifically, the 15° and 30° characteristic diffraction peaks of the orange curve correspond to the (100) and (200) plane, respectively. Additionally, there are small peaks contributed by (210) plane and (220) plane. It is evident that $CsPbBr_3$ is a polycrystalline film that is primarily dominated by (100) crystal plane. The XRD data for the ZnO film aligns well with the standard data card PDF#21-1486. The characteristic diffraction peak ≈34.4° displays a half-height and width close to 1°, indicating that the ZnO film possesses good crystallinity and orientation as a polycrystalline film. In conclusion, XRD analysis allows us to confirm that the crystallization characteristics of each film layer in the device meet the experimental design requirements.

Figure 3b presents PL spectra of ZnO film, Rubrene film, $CsPbBr_3$ film, and the device under 325 nm pulsed laser excitation. The data of ZnO film is represented by the purple curve, which exhibits a peak at ≈380 nm. This finding is consistent with previous literature, affirming a bandgap width of 3.26 eV. In the 500 to 580 nm region, yellow luminescence is detected, which caused by oxygen defects within the ZnO film, resulting in the transition of carriers between defect levels and semiconductor energy levels, producing wide fluorescence peaks. On the red curve, which corresponds to the photoluminescence of the Rubrene film, we observe a different behavior compared to inorganic materials. The Rubrene film has a minimal Stokes shift, making its detected emission spectrum easily influenced by self-absorption. At the shoulder of the strongest fluorescence peak, a significant emission can be observed. This may be due to wavelength-dependent scattering and reabsorption of emitted light. The main source of photoluminescence in organic matter is the amorphous phase. As the order of the film increases, the fluorescence intensity decreases. Therefore, the intensity of the strong main peak determines the film's amorphous properties. Moving to the orange curve, it represents the $CsPbBr_3$ film. The strongest fluorescence peak occurs at 525 nm and has a small

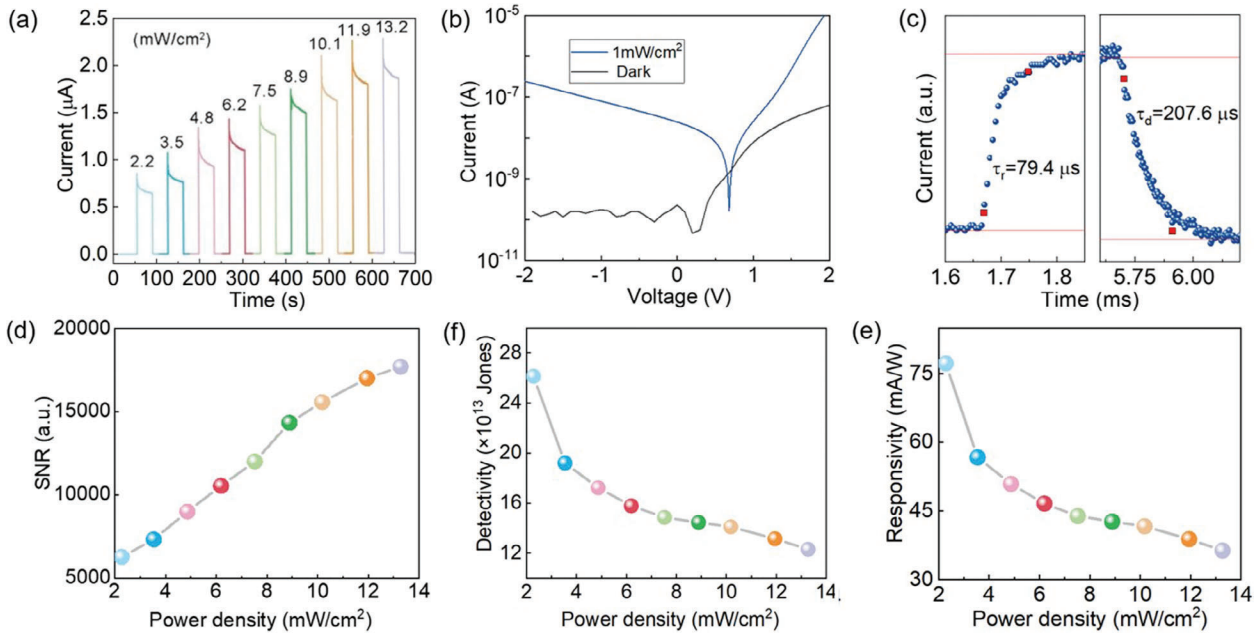

Figure 4. a) Photocurrent variation along with the power density. b) *I–V* curves and c) temporal photoresponse of a typical device measured in the dark and under 465 nm illumination. d) Signal to Noise Ratio, e) responsivity, and f) detectivity of the SPPDs at various illumination intensities.

half-height width. This indicates that the light-excited carriers primarily return to the ground state through radiation recombination. A low defect density and good crystallinity positively impact the generation and transport of photogenerated carriers, thereby enhancing the performance of photodetectors. The device composed of three layers of film exhibits two distinct fluorescence peaks when subjected to excitation light. However, due to the absorption of the Rubrene film and the $CsPbBr_3$ film, the PL peak of the ZnO film is not observable. Additionally, the separation of the light-excited carrier-hole pair by the functional layer leads to an evident quenching effect in the multilayer film. Consequently, the fluorescence peak intensity is significantly attenuated compared to that of the monolayer film.

Figure 3c shows the light absorption spectra of ZnO films, $CsPbBr_3$ films, Rubrene films, and devices deposited on an ITO/PET flexible substrate. The main function of a photodetector is to convert the absorbed light signal into an electrical signal. Therefore, understanding the light absorption characteristics of each layer of film in the detector is necessary. Inorganic materials mainly undergo intrinsic absorption, where the energy of photons is absorbed by the transition of electrons between the valence band and the conduction band. Consequently, the wavelength range of absorbed light depends solely on the band gap of the inorganic semiconductor material, irrespective of its defects or impurities. On the other hand, in organic semiconductors, light absorption is predominantly influenced by the optical properties and molecular arrangement within the crystal matrix, as well as the interaction between molecules. Consequently, the lattice characteristics of organic semiconductors significantly impact their absorption spectra. Polarized electrons in molecular orbitals are responsible for interacting with light and absorb the energy of photons during the transition from the lowest unoccupied molecular orbital (LUMO) to the highest occupied molecular orbital (HOMO). However, during this process, the interaction between molecular orbitals depolarizes the polarized electrons, leading to significant differences in light absorption intensity at different wavelengths. Comparatively, the absorption spectrum of the amorphous Rubrene film aligns closely with the curve reported in a previous article,[32] affirming that the Rubrene grown on the ITO/PET substrate is of good quality.

The responsivity of a detector at different wavelengths can be characterized using a UV–vis spectrophotometer. This analysis is then compared to the reference current output from a standard silicon detector. In Figure 3d, the data shows the detector's response to incident light. The response starts at 550 nm, reaches its highest value ≈465 nm, and gradually decreases thereafter. Moreover, the curve exhibits a similar trend to the absorption spectrum of the $CsPbBr_3$ film. Based on these observations, it can be preliminarily concluded that light absorption primarily takes place in the $CsPbBr_3$ layer. Meanwhile, the ZnO film and Rubrene film function as carriers transport layers.

Photocurrents and dark currents of device are acquired by the current–time (*I–t*) response test under 465 nm illumination of different power density on–off at 0 V. **Figure** 4a depicts the variation in photocurrent output of the detector under varying illuminations. The observation reveals a consistent pattern where an increase in light intensity corresponds to an increase in photocurrent. The voltage-current (*I–V*) curves of the detector are exhibited in Figure 4b. The test data, represented by the gray curve, indicates that the device is in a forward bias state at a voltage of 3 V, with a current of 2.2×10^{-7} A. Upon reversing the voltage, the current decreases significantly to 2.1×10^{-10} A, demonstrating a remarkable PN junction rectification effect. The rectification ratio is calculated to be 10^3. When the detector is illuminated with 465 nm light, the blue curve represents the corresponding data. By examining the position of the minimum current and the

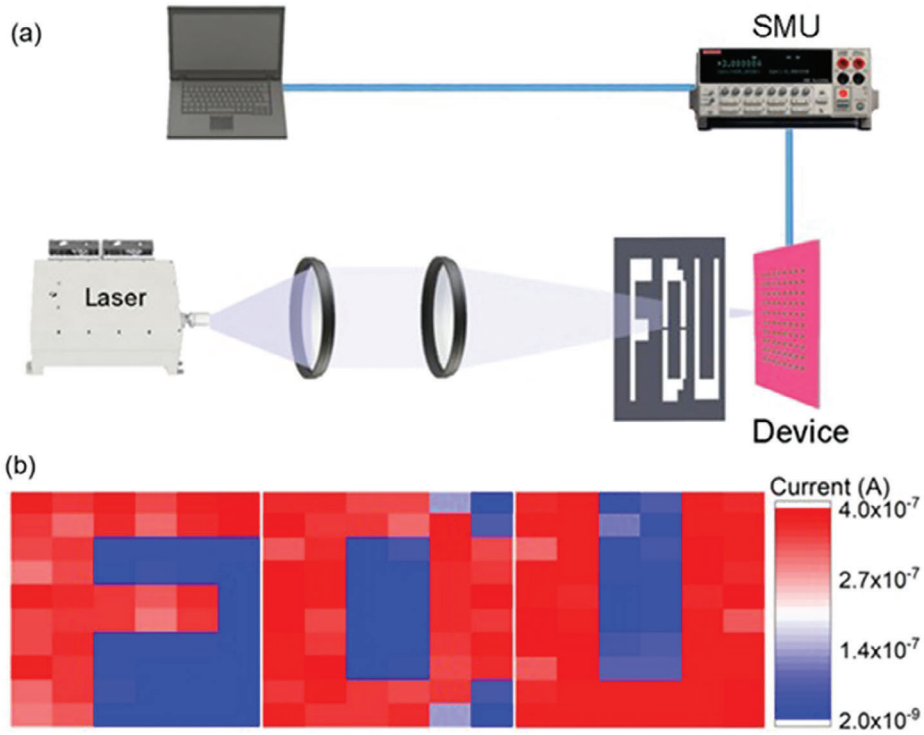

Figure 5. a) Schematic diagram of the imaging system based on SPPD. b) The imaging results of Fudan university logo "FDU" produced by 465 nm illumination.

current magnitude at 0 V, it can be inferred that incident light generates either a voltage of 0.68 V or a photocurrent of 2.7×10^{-8} A without the external bias. The response speed of SPPDs is a significant parameter that reflects the capability of the detector to track rapidly changing light signals. Rise time (τ_r) is defined as the time required for the photocurrent to increase from 10% to 90% of the maximum photocurrent, and fall time (τ_f) is the time to drop from 90% to 10% of the maximum photocurrent value. Response time of the flexible PD device is investigated at 0 V bias under periodically on/off 465 nm light irradiation. As shown in Figure 4c, τ_r and τ_f are found to be 79.4 µs and 207.6 µs, respectively.

To further evaluate the performance of SPPDs, three key figures of merit have been investigated, including Signal-to-noise ratio (SNR), responsivity (R), specific detectivity (D*). The dark current in SPPDs is determined by several factors. First, thermal excitation is a common cause of dark current generation, although it may not always occur directly from the valence to conduction band. Instead, it can be mediated through defect states associated with crystal defects or impurities, which results in a lower activation energy. Additionally, the temperature and band gap energy of the material, as well as the energy levels of common defects, critically influence the rate of these thermal processes. Thus, dark current is usually a relatively stable value, and the trend of SNR variation depends on the changes in photocurrent, and it can be defined as:[43]

$$\mathrm{SNR} = \frac{I_\mathrm{p}}{I_\mathrm{d}} \tag{2}$$

Here I_p and I_d represent the photocurrent and the dark current, respectively. As demonstrated in Figure 4d, the highest SNR is measured at 17700 at an incident light intensity of 13.2 mW cm^{-2}, while the lowest SNR is measured at 6270 under the weakest incident light condition. R represents the SPPDs' efficiency to convert light into electric current, which can be extracted by the following expression:[44,45]

$$R = \frac{I_p - I_d}{P_{in} \times S_d} \tag{3}$$

Where P_{in} is power density of the incident illumination, and S_d is the effective area of the PDs. As shown in Figure 4e, it can be observed that the responsivity decreases with the increase of light intensity. The maximum value is 77.2 mA W^{-1} under 2.2 mW cm^{-2} illumination, and when the light intensity increases, the responsivity decreases to 36 mA W^{-1}. This decreasing trend is due to the increased probability of radiation recombination and non-radiative recombination under strong light stimulation, leading to a decrease in responsiveness. According to the foregoing, the average dark current of the detector is 1.04×10^{-10} A. Using this data, the detectivity (D*) of the detector can be obtained by the following formula:[46]

$$D^* = \frac{\sqrt{A}R}{\sqrt{2qI_d}} \tag{4}$$

where q represents the elementary charge. As shown in Figure 4f. The trend of detection rate is consistent with the responsivity,

decreasing from 2.61×10^{13} Jones to 1.23×10^{13} Jones with increasing illumination.

Using Rubrene as the protective layer and hole transport layer not only enhances its stability but also simplifies the device structure. This makes it easier to construct complex electrode arrays to fulfill a wider range of application needs. To demonstrate the potential of these devices in practical scenarios, image sensor arrays are fabricated. In the array, 10 × 10 pixels can detect the edge features of incident light, and images can be obtained through data acquisition and computer processing. The schematic of the image sensing analysis system, which contains a laser unit, lens unit, metal mask, sensor array, source and measurement unit (SMU), and laptop, is displayed in **Figure** 5a. After passing through the lens unit, the incident light gradually sweeps the letters on the metal mask. At the same time, the SMU receives the photocurrent generated by the corresponding pixels in the detector array. The computer records the current value received by the SMU and draws pictures in turn. The resulting image is then colored according to the size of the current value, as shown in Figure 5b. These devices are particularly well-suited for applications such as irregularly shaped and wearable devices due to their ability to be easily processed, excellent flexibility, and performance.

3. Conclusion

In summary, the utilization of amorphous Rubrene films endows perovskite-based optoelectronic devices with water resistance and flexibility. This is mainly due to the high density and hydrophobicity of Rubrene films, which can prevent water molecules from entering the device interior and damaging perovskite films. PL spectra confirms that various perovskite films protected by Rubrene maintain their crystalline structure integrity even after prolonged immersion in water for 6000 min. Subsequently, $CsPbBr_3$ perovskite films are selected as the primary focus for research, and a Rubrene/$CsPbBr_3$/ZnO heterostructu\re device is fabricated on a flexible ITO/PET substrate. It is verified through systematic stability testing and characterization of optoelectronic performance that the Rubrene film not only enhances device stability but also contributes to their excellent optoelectronic photodetection capabilities. In addition, the potential application of such devices has been demonstrated by constructing an imaging array. This is because the absence of a packaging layer allows for the direct construction of complex electrode structures on the heterojunction surface. As a result, flexible devices can be quickly constructed, making them suitable for complex scenarios. Therefore, this amorphous organic film, which can serve as both a protective layer and a hole transport layer, provides a meaningful reference pathway for the construction of more stable and efficient perovskite optoelectronic devices.

4. Experimental Section

Growth of Metal Halide Perovskite Films: $MAPbBr_3$, $(PEA)_2PbBr_4$, $CsPbBr_3$, and $FAPbI_3$ powders were purchased from Xi'an Yuri Solar Co., Ltd. PVK films were prepared by PLD technique, using a solid-state Nd:YAG laser (λ = 355 nm, Nimma-900, Beamtech Optronics Co., Ltd.). The laser energy and repetition rate were fixed at 50 mJ and 1 Hz, respectively. During the deposition, the chamber vacuum was pumped down to 5×10^{-5} Pa and the substrate temperature was kept at 170 °C. The distance between target-substrate was 6.5 cm. Due to the significant negative impact of iodine on the high vacuum of PLD systems, the single-source vapor deposition (SSVD) method was employed to fabricate $FAPbI_3$ films. The chamber was pumped down to a base pressure of less than 1×10^{-3} Pa. The current applied to the tungsten wire was 25.2 A, and the deposition rate of the film was 0.3 Å s^{-1}.

SPPD Fabrication: ZnO films and PVK films were deposited on ITO/PET substrates with a metal mask via the PLD technique. Rubrene powder was purchased from Aladdin Co., Ltd. and thermally evaporated on the top of $CsPbBr_3$ film. Au electrode arrays were also deposited by thermal evaporation on the top of Rubrene films. The thickness of the films was monitored by deposition controller (SQC310, Filtech Inc.).

Characterization: The surface morphology was examined using a field-emission scanning electron microscope (FESEM, S4800, Hitachi Ltd.) and an atomic force microscope (Shimadzu Co.). The phase purity and crystallinity of the films were examined by an X-ray diffractometer (SmartLab, Rigaku Co.) with Cu Kα radiation (λ = 0.154 nm). The steady-state PL spectrum measurement was performed at room temperature by exciting the sample with a He-Cd laser (λ = 325 nm, Kimmon Koha Co.). A manual probe station equipped with a Source Meter (Keithley 2400), a picoammeter (Keithley 6487), a parameter analyzer (Keithley 4200-SCS), and a semiconductor laser (λ = 465 nm) was employed to record the photoresponse characteristics of the SPPDs. A homemade test system, containing a chopper (SR 540, SRS Inc.) and an oscilloscope (Tektronix MSO 3054) was used to investigate the response time. The imaging sensing performance was tested in a homemade probe station.

Supporting Information

Supporting Information is available from the Wiley Online Library or from the author.

Acknowledgements

The authors would like to thank Yuzhi Xing, Houning Song, Tingting Yan for their valuable discussions. This work is supported by National Natural Science Foundation of China (No. 92263106, 12061131009 and 12211530438), Science and Technology Commission of Shanghai Municipality (No. 21520712600 and 19520744300).

Conflict of Interest

The authors declare no conflict of interest.

Data Availability Statement

The data that support the findings of this study are available from the corresponding author upon reasonable request.

Keywords

amorphous organic, flexible photodetector, perovskite, stability, self-powered

Received: October 3, 2023
Revised: December 16, 2023
Published online:

[1] C. P. Veeramalai, S. Feng, X. Zhang, S. V. N. Pammi, V. Pecunia, C. Li, *Photonics Res.* **2021**, *9*, 968.

[2] F. Wang, X. Zou, M. Xu, H. Wang, H. Wang, H. Guo, J. Guo, P. Wang, M. Peng, Z. Wang, Y. Wang, J. Miao, F. Chen, J. Wang, X. Chen, A. Pan, C. Shan, L. Liao, W. Hu, *Adv. Sci.* **2021**, *8*, 2100569.
[3] D. Saikia, A. Betal, J. Bera, S. Sahu, *Mater. Sci. Semicon. Process.* **2022**, *150*, 106953.
[4] F. Cao, Z. Hu, T. Yan, E. Hong, X. Deng, L. Wu, X. Fang, *Adv. Mater.* **2023**, *35*, 2304550.
[5] X. Chu, Q. Ye, Z. Wang, C. Zhang, F. Ma, Z. Qu, Y. Zhao, Z. Yin, H.-X. Deng, X. Zhang, J. You, *Nat. Energy* **2023**, *8*, 372.
[6] S.-J. Woo, J. S. Kim, T.-W. Lee, *Nat. Photonics* **2021**, *15*, 630.
[7] L. Lei, Q. Dong, K. Gundogdu, F. So, *Adv. Funct. Mater.* **2021**, *31*, 2010144.
[8] D. Liu, B.-B. Yu, M. Liao, Z. Jin, L. Zhou, X. Zhang, F. Wang, H. He, T. Gatti, Z. He, *ACS Appl. Mater. Interfaces* **2020**, *12*, 30530.
[9] D. Wu, Y. Xu, H. Zhou, X. Feng, J. Zhang, X. Pan, Z. Gao, R. Wang, G. Ma, L. Tao, H. Wang, J. Duan, H. Wan, J. Zhang, L. Shen, H. Wang, T. Zhai, *InfoMat* **2022**, *4*, e12320.
[10] Z. Li, E. Hong, X. Zhang, M. Deng, X. Fang, *J. Phys. Chem. Lett.* **2022**, *13*, 1215.
[11] C. C. Boyd, R. Cheacharoen, T. Leijtens, M. D. Mcgehee, *Chem. Rev.* **2018**, *119*, 3418.
[12] Z. Zhu, Q. Sun, Z. Zhang, J. Dai, G. Xing, S. Li, X. Huang, W. Huang, *J. Mater. Chem. C* **2018**, *6*, 10121.
[13] Z. Gao, H. Zhou, K. Dong, C. Wang, J. Wei, Z. Li, J. Li, Y. Liu, J. Zhao, G. Fang, *Nano-Micro Lett.* **2022**, *14*, 215.
[14] A. Aftab, M.. I. Ahmad, *Sol. Energy* **2021**, *216*, 26.
[15] G. Y. Kim, A. Senocrate, T.-Y. Yang, G. Gregori, M. Grätzel, J. Maier, *Nat. Mater.* **2018**, *17*, 445.
[16] T. Leijtens, E. T. Hoke, G. Grancini, D. J. Slotcavage, G. E. Eperon, J. M. Ball, M. De Bastiani, A. R. Bowring, N. Martino, K. Wojciechowski, M. D. Mcgehee, H. J. Snaith, A. Petrozza, *Adv. Energy Mater.* **2015**, *5*, 1500962.
[17] Z. Wang, Z. Shi, T. Li, Y. Chen, W. Huang, *Angew. Chem., Int. Ed.* **2017**, *56*, 1190.
[18] P. Wang, X. Zhang, Y. Zhou, Q. Jiang, Q. Ye, Z. Chu, X. Li, X. Yang, Z. Yin, J. You, *Nat. Commun.* **2018**, *9*, 2225.
[19] N. Rolston, K. A. Bush, A. D. Printz, A. Gold-Parker, Y. Ding, M. F. Toney, M. D. Mcgehee, R. H. Dauskardt, *Adv. Energy Mater.* **2018**, *8*, 1802139.
[20] S. Yang, L. Wang, L. Gao, J. Cao, Q. Han, F. Yu, Y. Kamata, C. Zhang, M. Fan, G. Wei, T. Ma, *ACS Appl. Mater. Interfaces* **2020**, *12*, 13931.
[21] G.-B. Xiao, Z.-F. Yu, J. Cao, Y. Tang, *CCS Chem.* **2020**, *2*, 488.
[22] R. K. Raman, S. A. G. Thangavelu, S. Venkataraj, A. Krishnamoorthy, *Renewable Sustainable Energy Rev.* **2021**, *151*, 111608.
[23] S. Jiang, K. Wang, H. Zhang, Y. Ding, Q. Yu, *Macromol. React. Eng.* **2015**, *9*, 522.
[24] S. Ma, Y. Bai, H. Wang, H. Zai, J. Wu, L. Li, S. Xiang, N. Liu, L. Liu, C. Zhu, G. Liu, X. Niu, H. Chen, H. Zhou, Y. Li, Q. Chen, *Adv. Energy Mater.* **2020**, *10*, 1902472.
[25] Z. Liu, B. Sun, T. Shi, Z. Tang, G. Liao, *J. Mater. Chem. A* **2016**, *4*, 10700.
[26] C.-H. Chen, P.-H. Sher, C.-P. Chen, W.-K. Choi, C. J. Bardeen, T.-L. Chiu, J.-K. Wang, J.-H. Lee, *J. Phys. Chem. C* **2020**, *124*, 25729.
[27] C.-J. Park, H. J. Park, J. Y. Lee, J. Kim, C.-H. Lee, J. Joo, *ACS Appl. Mater. Interfaces* **2018**, *10*, 29848.
[28] W. Hu, K. Sun, Q. Xu, L. Chen, Y. Zhao, *J. Chem. Phys.* **2020**, *153*, 174105.
[29] L. Chen, J. Deng, H. Gao, Q. Yang, L. Kong, M. Cui, Z. Zhang, *Appl. Surf. Sci.* **2016**, *388*, 396.
[30] C.-J. Park, H. J. Park, J. Y. Kim, S.-H. Lee, Y. Lee, J. Kim, J. Joo, *Semicond. Sci. Technol.* **2020**, *35*, 065020.
[31] W.-C. Su, C.-C. Lee, Y.-Z. Li, S.-W. Liu, *ACS Appl. Mater. Interfaces* **2016**, *8*, 28757.
[32] J. Euvrard, O. Gunawan, A. Kahn, B. P. Rand, *Adv. Funct. Mater.* **2022**, *32*, 2206438.
[33] B. Li, M. Wang, R. Subair, G. Cao, J. Tian, *J. Phys. Chem. C* **2018**, *122*, 25260.
[34] J. Idígoras, F. J. Aparicio, L. Contreras-Bernal, S. Ramos-Terrón, M. Alcaire, J. R. Sánchez-Valencia, A. Borras, Á. Barranco, J. A. Anta, *ACS Appl. Mater. Interfaces* **2018**, *10*, 11587.
[35] Q. Dong, F. Liu, M. K. Wong, H. W. Tam, A. B. Djurisic, A. Ng, C. Surya, W. K. Chan, A. M. C. Ng, *Chem* **2016**, *9*, 2597.
[36] J. Fan, Y. Ma, C. Zhang, C. Liu, W. Li, R. E. I. Schropp, Y. Mai, *Adv. Energy Mater.* **2018**, *8*, 1703421.
[37] M. Wang, H. Sun, F. Cao, W. Tian, L. Li, *Adv. Mater.* **2021**, *33*, 2100625.
[38] T. Shi, X. Chen, R. He, H. Huang, X. Yuan, Z. Zhang, J. Wang, P. K. Chu, X.-F. Yu, *Adv. Sci.* **2023**, *10*, 2302005.
[39] A. J. Leo, *Methods Enzymol.* **1991**, *202*, 544.
[40] Y. Yao, C. Cheng, C. Zhang, H. Hu, K. Wang, S. De Wolf, *Adv. Mater.* **2022**, *34*, 2203794.
[41] X. Cheng, K. W. Putz, C. D. Wood, L. C. Brinson, *Macromol. Rapid Commun.* **2015**, *36*, 391.
[42] Y.-W. Jhou, C.-K. Yang, S.-Y. Sie, H.-C. Chiu, J.-S. Tsay, *Phys. Chem. Chem. Phys.* **2019**, *21*, 4939.
[43] R. Xing, P. Shi, D. Wang, Z. Wu, Y. Ge, Y. Xing, L. Wei, S. Yan, Y. Tian, L. Bai, Y. Chen, *ACS Appl. Mater. Interfaces* **2022**, *14*, 40093.
[44] Z. Li, Z. Li, C. Zuo, X. Fang, *Adv. Mater.* **2022**, *34*, 2109083.
[45] Y. Chen, L. Su, M. Jiang, X. Fang, *J. Mater. Sci. Technol.* **2022**, *105*, 259.
[46] F. Cao, T. Yan, Z. Li, L. Wu, X. Fang, *Adv. Opt. Mater.* **2022**, *10*, 2200786.